Materials Advances

ROYAL SOCIETY OF CHEMISTRY

PAPER

View Article Online
View Journal

Cite this: DOI: 10.1039/d6ma00062b

Grain structure–controlled growth of InSb crystals: a grain boundary engineering approach for enhanced thermoelectric performance

M. Sivakumar, [a] J. Prasath,[a] S. Senthamizh Raja,[a] R. Annie Victoria Rose,[a] J. Mani,[b] L. C. Chuang,[c] Sri Sai Samhitha Gadhavajhala,[d] Bhuvanesh Srinivasan, [d] R. Jayavel, [e] K. Fujiwara[c] and M. Arivanandhan *[a]

Received 14th January 2026,
Accepted 7th May 2026

DOI: 10.1039/d6ma00062b

rsc.li/materials-advances

InSb polycrystalline ingots were prepared using the direct melt quenching method at different cooling rates: slow cooling (SC), air quenching (AQ), and ice water quenching (IWQ). The crystal structure and grain structure of the InSb ingots were analysed by XRD and FESEM. The variations in the grain structure, grain orientation, and grain boundaries of the samples with different cooling rates were analysed by EBSD. The Seebeck coefficient (S) of the InSb samples decreased with increasing cooling rates owing to a slight decrease in the electrical resistivity. A high-power factor (PF) of 6951 μW m^{-1} K^{-2} was achieved for the IWQ sample at 573 K compared to the SC InSb sample (5935 μW m^{-1} K^{-2} at 573 K). The thermal conductivity decreased for the IWQ InSb sample (6.60 W m^{-1} K^{-1} at 573 K) compared to SC InSb (7.29 W m^{-1} K^{-1} at 573 K) due to the modifications in the grain structures, grain boundary densities and grain boundary characteristics of InSb during rapid cooling, which enhanced the phonon scattering in the IWQ sample. Subsequently, a high zT value of 0.60 was achieved at 573 K for the IWQ InSb sample compared to the SC InSb sample (zT of 0.46 at 573 K).

1. Introduction

Electrical energy is very significant for all sectors in this modern world. The demand for electric energy is rapidly increasing due to the increasing global human population.[1] Furthermore, the high amount of burning of fossil fuels emits CO_2, which leads to an increase in global warming.[2,3] Hence, an alternative and sustainable energy source is needed to fulfil the energy requirement as well as the energy demand. Such a kind of clean energy is more important for a green and pollution-free environment to realize sustainable developments.[4–6] In industries and automobiles, a lot of energy remains unused in the form of heat energy.[7,8] Thermoelectric (TE) technology is a promising technology for converting this kind of waste heat into useful electricity through the principle of the Seebeck effect.[9,10] A thermoelectric device consists of p-type and n-type materials connected electrically in series and thermally in parallel. TE technology is pollution-free and environmentally friendly, with non-movable parts that offer practical operational integration.[11] TE technology is useful in various applications, such as thermoelectric generators, wearable watches, Peltier modules, sensors, and electronic gadgets. The performance of a TE functional material is based on the figure of merit (zT), as shown in the following equation:

$$zT = \frac{S^2}{\rho \kappa_T} T, \quad (1)$$

where S is the Seebeck coefficient, ρ is the electrical resistivity, κ_T is the total thermal conductivity, and T is the absolute temperature.[12] A good thermoelectric material should have $zT > 1$ to be suitable for practical applications. A high zT can be attained by increasing the power factor (PF) $\left(\mathrm{PF} = \frac{S^2}{\rho}\right)$ and reducing the thermal conductivity.[13] The PF can be enhanced by hetero valence substitution,[14,15] doping,[12,16,17] compositing,[18–20] and nano-inclusions.[21–23] Thermal conductivity can be suppressed through nano-structuring[24–26] of the material, defect engineering,[27–29] point defect scattering,[27,28] grain boundary engineering,[30,31] phonon engineering,[24,32–35] and melt quenching.[32,36] Good thermoelectric materials behave like phonon glass–electron crystal (PGEC).[33] However, in general, the thermal and electrical conductivities are coupled. Therefore, it is quite difficult to enhance the

[a] Centre for Nanoscience and Technology, Anna University, Chennai-600 025, Tamil Nadu, India. E-mail: arivucz@gmail.com
[b] MoE Key Laboratory of Material Physics and Chemistry Under Extraordinary Conditions, School of Physical Science and Technology, Northwestern Polytechnical University, Xi'an – 710072, People's Republic of China
[c] Institute for Materials Research, Tohoku University, Sendai – 980 8577, Japan
[d] Department of Metallurgical and Materials Engineering, Indian Institute of Technology Madras (IIT-Madras), Chennai 600 036, Tamil Nadu, India
[e] Crystal Growth Centre, Anna University, Chennai-600 025, Tamil Nadu, India

performance of TE energy harvesting materials by decoupling their electrical and thermal conductivities. Semiconductors are suitable materials for improving the zT value of the material[37] because semiconductors have optimum carrier concentrations and tunable bandgaps as well as low thermal conductivity.[38] A lot of semiconductor materials exhibit high TE performance. Bi_2Te_3[36,37] and $Si_{1-x}Ge_x$[39] are familiar semiconductor materials for low- and high-temperature TE applications, respectively. However, an appropriate functional material for mid-temperature TE applications is still lacking, despite the high performance of a few materials such as SnSe and GeTe.[40,41]

InSb is a narrow bandgap semiconductor with a bandgap of 0.18 eV, making it suitable for TE applications.[42] The material has high mobility (μ) and carrier concentration (n) in the range of 10^4–10^5 cm^2 V^{-1} S^{-1} and $\sim 10^{17}$ cm^{-3}, respectively.[43,44] Besson *et al.* prepared sphalerite-structured InSb nanoparticles by alloying Sb with indium nano clusters.[45] Cheng *et al.* reported melt-quenched polycrystalline $InSb_{1.04}$ ingots with a zT value of 1.28 at 773 K.[46] Min Jin *et al.* prepared InSb ingots using the Bridgman technique and achieved a zT of 0.63 at 700 K.[44] Kang Wang *et al.* reported a zT value of 0.4 for a melt-quenched InSb sample.[47] Yamaguchi *et al.* achieved a zT value of 0.60 at 673 K, which was grown using the Czochralski method.[48] Kaiqi Zhang *et al.* reported the $AgSb_{0.973}Cd_{0.017}Se_2$ crystal with a high thermoelectric zT value of 1.7 at 723 K using the Bridgman crystal growth technique.[31] Qi-Qi Wang *et al.* reported a high zT value of ~ 0.9 at 300 K and an excellent average zT value of 1.26 using the *in situ* loading Bridgman growth method.[30] However, the high thermal conductivity ($\sim$16–18 W m^{-1} K^{-1} at 300 K) affects the zT of InSb material, which limits its practical applications.[46] Therefore, it is essential to reduce the thermal conductivity of InSb to enhance zT.[49,50] Developing new strategies, like nanostructuring,[51] grain boundary engineering,[30,31] and nano inclusions,[52] are the imperative techniques for suppressing the thermal conductivity of InSb. Among these strategies, rapid melt quenching is one of the bulk preparation processes used to prepare InSb with controlled grain structures. This technique effectively controls the grain structure and, consequently, the grain boundaries. The grain boundaries are the active regions for controlling thermal conductivity through effective phonon scattering. The manipulation of the grain boundaries through the crystallization process is an effective strategy for enhancing the zT value. However, this approach has not yet been systematically investigated for InSb. Therefore, in the present study, InSb was crystallized by applying the melt quenching technique at different cooling rates to manipulate its grain structures. The structural, morphological and thermoelectric properties of the melt-quenched InSb ingots were evaluated. By optimizing the grain structure, the TE performance was greatly enhanced with low thermal conductivity. The thermal conductivity is effectively reduced for the IWQ InSb sample (6.60 W m^{-1} K^{-1} at 573 K) compared to SC InSb (7.29 W m^{-1} K^{-1} at 573 K) due to the modification of the grain structures and grain boundary densities, which enhanced the phonon scattering in the IWQ sample. Subsequently, a high zT of 0.60 was achieved at 573 K for the IWQ InSb sample compared to the SC InSb sample (zT of 0.46 at 573 K). The experimental results highlight a simple and scalable microstructural engineering strategy and establish InSb as a useful material for high-performance thermoelectric systems.

2. Experimental section

2.1 Materials

InSb polycrystals were prepared using the direct melt quenching technique at different cooling rates. High-purity source materials of indium shots (6 N purity) and antimony shots (6 N purity) were purchased from Osaka Chemicals, Japan. The stoichiometric equimolar ratio of (1 : 1) In and Sb was loaded into a cylinder-shaped quartz ampoule (16 mm inner diameter × 20 mm outer diameter × 15 cm length), and the ampoule was evacuated under the vacuum pressure of 10^{-5} Torr. Then the sealed quartz ampoule was kept in a high-temperature furnace. The temperature of the furnace was increased from 35 to 640 °C at a ramping rate of 5 °C min^{-1} and dwelled at 640 °C for 15 hours to achieve homogeneous melting of the indium and antimony shots. After homogeneous melting, the ampoule with the molten sample was cooled at a cooling rate of 1 °C min^{-1} to prepare the sample under slow cooling. Similarly, the other two ampoules with In and Sb samples were sealed and melted under identical conditions. After the dwelling period, the ampoules were drastically cooled by air quenching and ice water quenching processes. After the growth experiment, the InSb ingots were cut and polished into rectangular and circular-shaped samples. These samples were used to measure the TE properties at different temperatures. The prepared slow-cooled, air-quenched, and ice water-quenched samples were named SC InSb, AQ InSb and IWQ InSb, respectively. A schematic diagram of the InSb sample preparation procedure is shown in Fig. 1(a). The thermal cycling program used for crystallization at different cooling rates is shown in Fig. 1(b).

2.2 Characterization

The physicochemical and thermoelectric properties of polycrystalline InSb samples were characterized using various physicochemical characterization techniques, such as X-ray diffraction (XRD), field emission scanning electron microscopy (FESEM), energy dispersive X-ray spectroscopy (EDX), electron back scatter diffraction (EBSD), Raman spectroscopy, X-ray photoelectron spectroscopy (XPS), Hall measurements, Seebeck coefficient, and thermal diffusivity measurements. XRD was used to characterize the phase purity and crystal structures of the prepared samples. The analysis was performed using a Bruker D8 advance X-ray diffractometer (Japan) with Cu Kα1 radiation (λ = 1.5406 Å). FESEM and EDX analyses revealed the surface grain structure and elemental composition. These analyses were performed using a Carl-Zeiss instrument. Raman spectroscopy analysis was performed to examine the vibrational properties of the InSb samples. A RENISHAW instrument (UK), equipped with a 532 nm laser and a CCD array NIR detector, was used for the analysis. X-ray photoelectron spectroscopy (XPS) was used to determine the chemical binding states of the samples using a ULVAC instrument. Hall effect measurements were performed to determine the

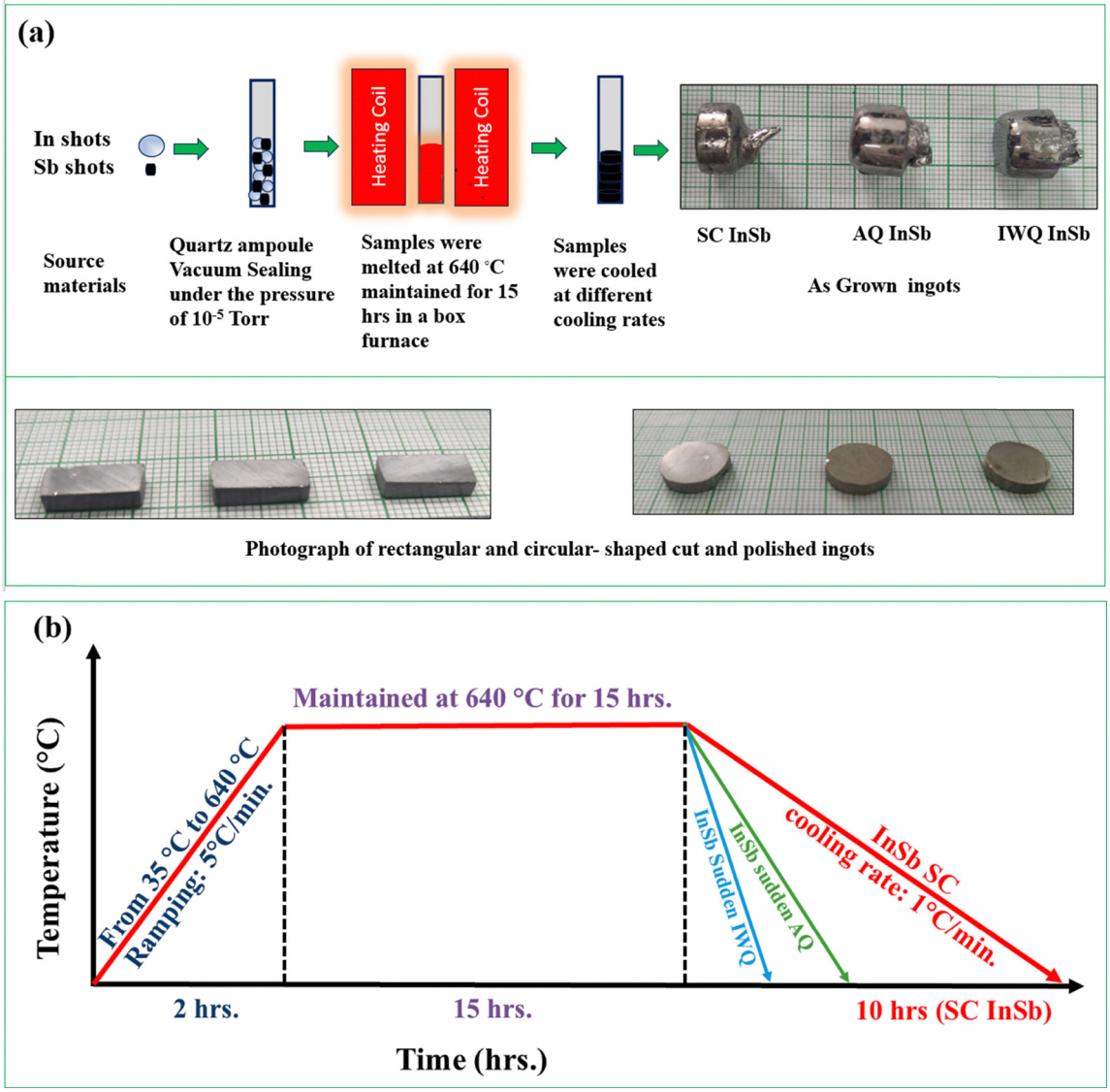

Fig. 1 Schematic of the sample preparation process (a) and thermal cycling program (b).

electrical properties, such as the carrier concentration and mobility, of the samples using an EXCEL India instrument. The Seebeck coefficient and electrical resistivity were measured using a ZEM 3 instrument (Advance Riko, Japan). Thermal diffusivity was determined using the laser flash technique with a Netzsch LFA-457 instrument under an argon gas atmosphere. These combined techniques provided a detailed understanding of the structural, morphological, electrical and thermal characteristics of the prepared InSb samples. The densities of all samples were calculated for cylindrical-shaped ingots. The achieved relative densities of SC, AQ and IWQ InSb are 89.1%, 87.2% and 85.3%, respectively.

3. Results and discussion

3.1 Structural analysis of InSb samples

Fig. 2(i)(a) shows the XRD pattern of the InSb ingots, which confirms the space group of *F*-43*m* with a cubic crystal structure of the InSb ingots. The obtained diffraction peak positions are 23.84°, 39.45°, 46.61°, 56.25°, 62.76°, 71.65°, and 76.77° for the corresponding planes (111), (220), (311), (400), (331), (422), and (511), respectively. All the diffraction peak positions are fine-matched with JCPDS card no. 06-0208.[44,53,54] Fig. 2(b) shows an enlarged and closer view of the most intense peak *hkl* value of (111). The intensity of the peak is suppressed for the rapidly cooled samples (AQ InSb and IWQ InSb) compared to the slow-cooled one (SC InSb). Moreover, the peaks are relatively broadened for the AQ InSb and IWQ InSb samples, which is mainly due to the higher lattice strain induced by rapid cooling. Ice-water quenching causes rapid cooling that suppresses atomic rearrangement, thereby freezing in fast-growing orientations, such as the (311) planes. This results in a preferred (311) texture and an enhanced (311) diffraction peak intensity. The crystallite sizes (D) were calculated using the following Scherrer's eqn (2):

$$D = \frac{0.9\lambda}{\beta \cos\theta}, \quad (2)$$

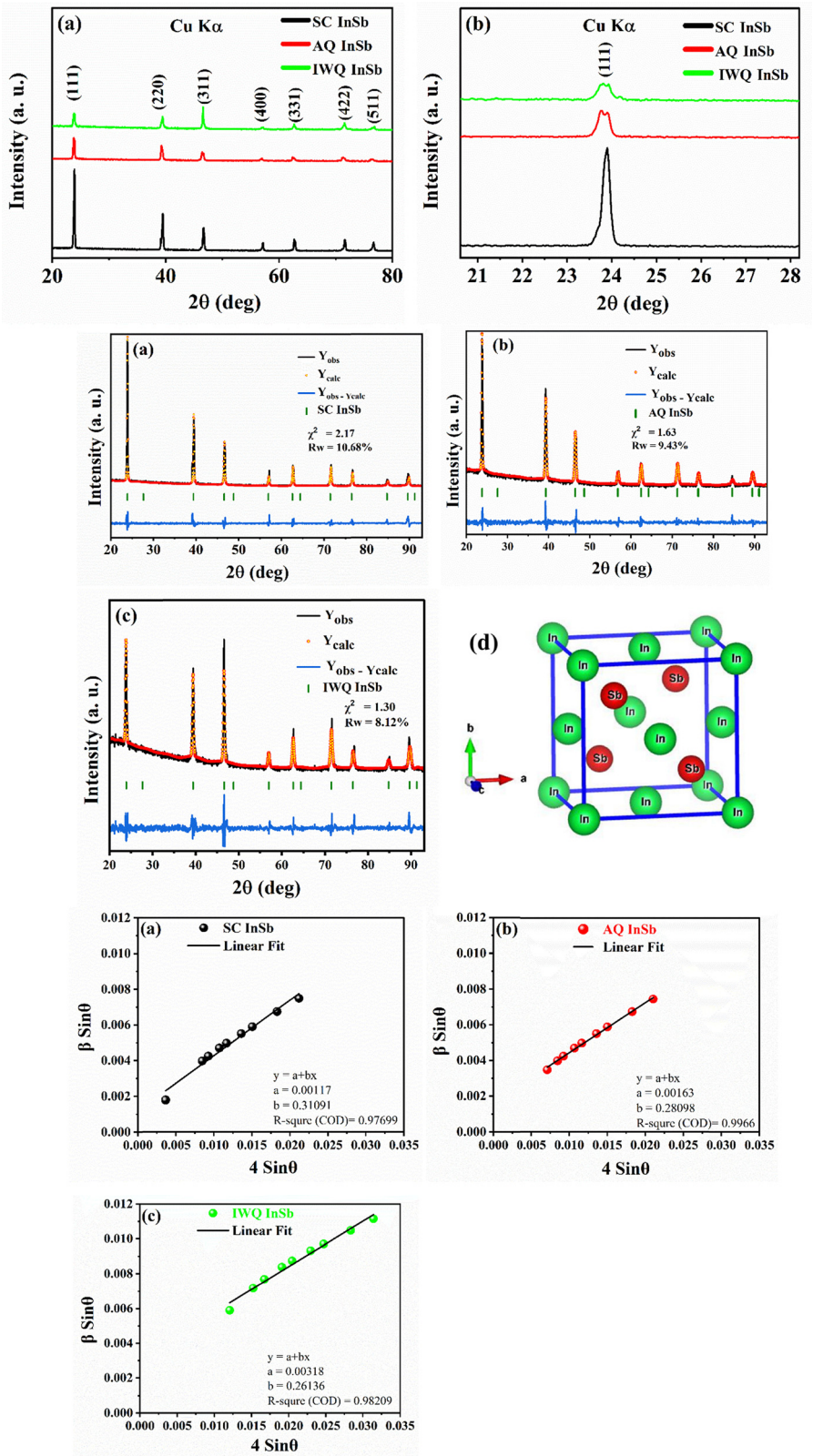

Fig. 2 (i) XRD diffraction patterns of InSb polycrystalline materials at various cooling rates (a) and a closer view of the XRD patterns of the (111) plane (b). (ii) Rietveld refinement of InSb samples of SC InSb (a), AQ InSb (b), IWQ InSb (c) and crystal structure (d) samples. (iii) Williamson–Hall plot of SC InSb (a), AQ InSb (b), and IWQ InSb (c) of InSb samples.

Table 1 Lattice parameter, lattice strain and crystallite size of InSb samples at different cooling rates

InSb with cooling rates	Lattice parameter (Å)	Crystallite size (nm)	Lattice micro strain
SC	6.47	118.5	0.3109
AQ	6.47	85.0	0.2809
IWQ	6.50	43.6	0.2613

where D is the crystallite size, λ is the X-ray wavelength (1.5406 Å), β is the full width at half maximum (FWHM) and θ is the diffraction angle. The lattice strain (β) was calculated using the following equation:

$$\varepsilon = \frac{\beta}{4\tan\theta}. \quad (3)$$

The lattice strain and related defects in the crystals facilitate phonon scattering, which is beneficial for controlling heat transport. The calculated lattice parameters, lattice micro strain, and crystallite size are listed in Table 1.

Fig. 2(ii) shows the Rietveld refinement of various cooled samples. The refinement validates the observed changes in lattice parameters and phase purity of SC InSb (a), AQ InSb (b), and IWQ InSb (c) samples. Fig. 2(iii) shows the Williamson–Hall (W–H) plots of SC InSb (a), AQ InSb (b), and IWQ InSb (c) and the crystal structure (d) of InSb samples. From the W–H plot, the lattice strain and crystallite size were calculated. The crystallite size decreased as the cooling rate increased mainly due to reduced grain growth. The lattice micro strain slightly decreased as the cooling rate increased due to faster cooling, which can suppress prolonged atomic diffusion. The calculated crystallite size and lattice strain are tabulated in Table 1.

3.2 Morphological analysis of the prepared InSb samples

Fig. S1(a_1)–(c_3) shows the FESEM images of the prepared ingots: SC InSb (a_1)–(a_3), AQ InSb (b_1)–(b_3), and IWQ InSb (c_1)–(c_3) samples. Fig. S2 illustrates EDX analysis of SC InSb (a), AQ InSb (b) and IWQ InSb (c) samples. The EDX spectrum confirms the presence of In and Sb for each sample. The elemental compositions of all the samples are illustrated in Table T1 (SI). Fig. S3 depicts the elemental mapping of SC InSb (a_1–a_4), AQ InSb (b_1–b_4), and IWQ InSb (c_1–c_4) samples.

Fig. 3 shows the FESEM images and EBSD orientation mappings of the SC InSb (a_1) and (a_2), AQ InSb (b_1) and (b_2), and IWQ InSb (c_1) and (c_2) samples with colored standard triangles of orientations. Fig. 3(a_1), (b_1) and (c_1) were obtained from the centre parts, and Fig. 3(a_2), (b_2) and (c_2) were obtained from the periphery parts of each sample. The EBSD analysis shows the crystallographic grain structure of the InSb samples with clear grain size variations in all the samples at different cooling rates. The EBSD analysis revealed grain growth as the cooling rates increased. During the quenching process, the molten InSb solidified rapidly as a function of the cooling rate. From the EBSD analysis, the average grain sizes at the centre and edge of the samples were found to be 910 μm and 905 μm in SC InSb, 467 μm and 482 μm in AQ InSb, and 213 μm and 158 μm in IWQ InSb, respectively. The coloured standard stereotype triangle shows the different orientations in the grains. During the quenching process, a large number of nucleations were formed in the molten InSb and grew rapidly, which restricted grain growth and resulted in fine grain structures. Therefore, the number of grain boundaries increased in IWQ InSb when compared to SC InSb. The grain boundary character distributions of SC InSb, AQ InSb and IWQ InSb samples are shown in Table S4(a)–(c). From Table S4(a), it is obvious that the low angle Σ3 and Σ9 grain boundaries were mainly observed in SC InSb. Table S4(b) shows the grain boundary characteristics of the AQ InSb sample. In the AQ InSb sample, the low angle grain boundaries of Σ3, Σ9 and higher angle grain boundaries of Σ27a, Σ27b, and Σ19a were observed. These mixed grain boundaries facilitate the effective scattering of the long-range phonon. Table S4(c) shows the grain boundary characteristics of the IWQ InSb sample. In the IWQ InSb sample, the low angle grain boundaries of Σ3, Σ9 and higher angle grain boundaries of Σ27a, Σ27b, Σ35b, and Σ19b were observed. In this sample, a higher amount of higher angle grain boundaries was present compared to the other samples. These higher angle grain boundaries facilitate effective scattering of the phonons, resulting in low κ_T.

3.3 Raman analysis of the InSb samples

Fig. 4 shows the Raman spectra of SC InSb (a), AQ InSb (b), and IWQ InSb (c) recorded in the Raman shift range of 111–300 cm^{-1}. The spectra exhibit characteristic vibrational features corresponding to the longitudinal optical (LO) and transverse optical (TO) phonon modes of InSb. For SC InSb, Raman peaks are observed at 108 cm^{-1} (A_{1g}), 143 cm^{-1} (A_{1g}), and 177 cm^{-1} (B_{1g}). The AQ InSb sample shows similar modes at 107 cm^{-1} (A_{1g}), 143 cm^{-1} (A_{1g}), and 178 cm^{-1} (B_{1g}). In contrast, IWQ InSb exhibits Raman peaks at 105 cm^{-1} (A_{1g}), 140 cm^{-1} (A_{1g}), 179 cm^{-1} (B_{1g}), and an additional LO mode at 188 cm^{-1} (A_{1g}). All observed Raman modes are in good agreement with previously reported literature values for crystalline InSb,[34,53] confirming the successful formation of the InSb phase. The Raman peaks corresponding to the rapidly cooled samples exhibit noticeable broadening and enhanced intensity, which can be attributed to lattice strain and disorder-induced relaxation of Raman selection rules, leading to modified phonon vibrational behaviour. The comparatively higher strain in IWQ InSb, inferred from the pronounced LO mode and peak broadening is consistent with the XRD results summarized in Table 1, indicating increased lattice distortion caused by rapid quenching.

3.4 Electrical transport properties of InSb prepared at different cooling rates

The ρ of the InSb samples with respect to temperature is shown in Fig. 5(a). The ρ of all samples decreased with increasing temperature, confirming the semiconductor behaviour of the sample. The ρ was slightly decreased while increasing the cooling rate. The ρ was slightly decreased from 2.74×10^{-5} Ω m (SC InSb sample) to 2.41×10^{-5} Ω m (IWQ InSb sample) at 319 K (Fig. 5(a)). Fig. 5(b) shows the variation in n of the prepared InSb

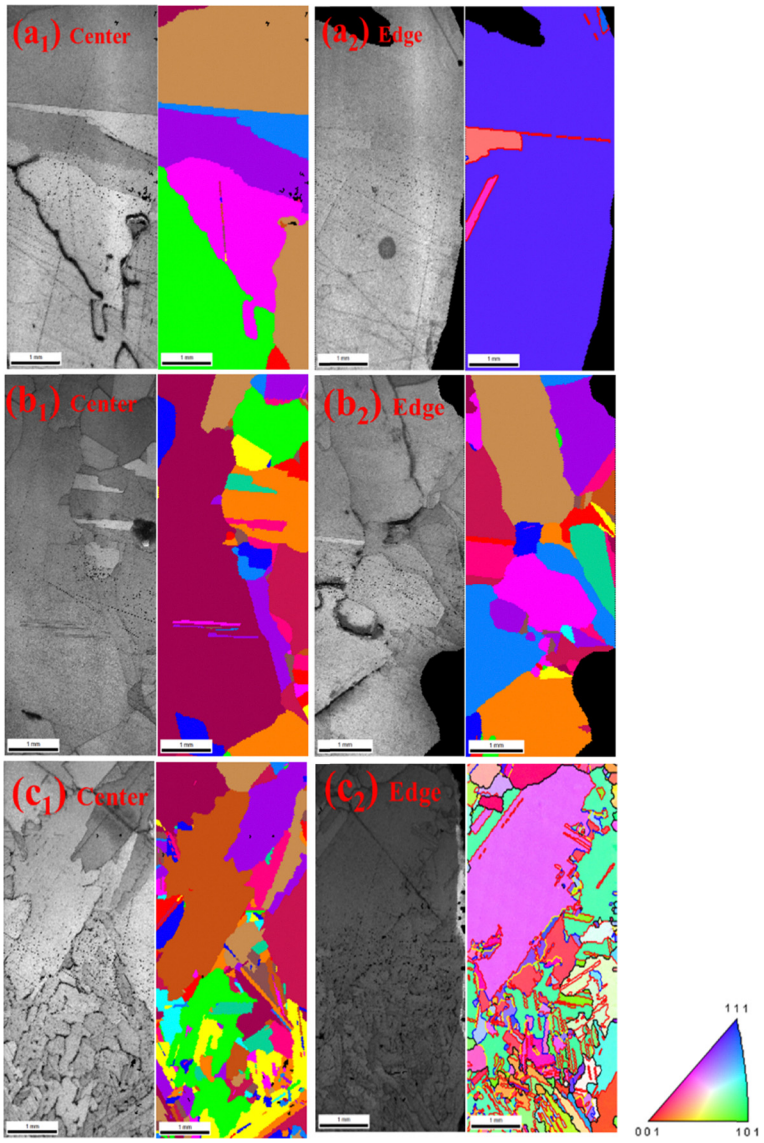

Fig. 3 EBSD images of SC InSb (a_1 – center, a_2 – periphery), AQ InSb (b_1 – center, b_2 – periphery), and IWQ InSb (c_1 – center, c_2 – periphery) samples with a colored standard triangle of orientation.

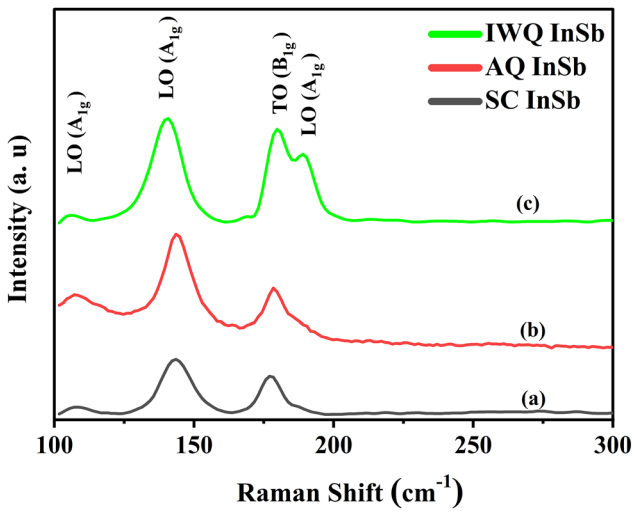

Fig. 4 Raman spectra of SC InSb (a), AQ InSb (b), and IWQ InSb (c) samples.

samples. The n was almost in the same order of 10^{17} cm^{-3} for all the InSb samples (Fig. 5(b)). The μ of InSb slightly increased from 1280 $cm^2 V^{-1} s^{-1}$ (SC InSb) to 1508 $cm^2 V^{-1} s^{-1}$ (IWQ InSb) while increasing the cooling rates (Fig. 5(c)). The slight decrease in ρ with an increasing cooling rate is possibly due to the presence of higher angle grain boundaries in the rapidly cooled samples, as observed in the EBSD analysis. The higher angle grain boundaries result in higher μ in the samples, leading to low resistivity in the rapidly cooled samples despite the same range of n values.

3.5 Seebeck coefficient of InSb samples

Fig. 6 shows the Seebeck coefficients (S) of all the InSb ingots as a function of temperature. The S values of all the InSb samples show negative values, indicating that all the prepared samples have n-type semiconducting behaviour. The S value decreased

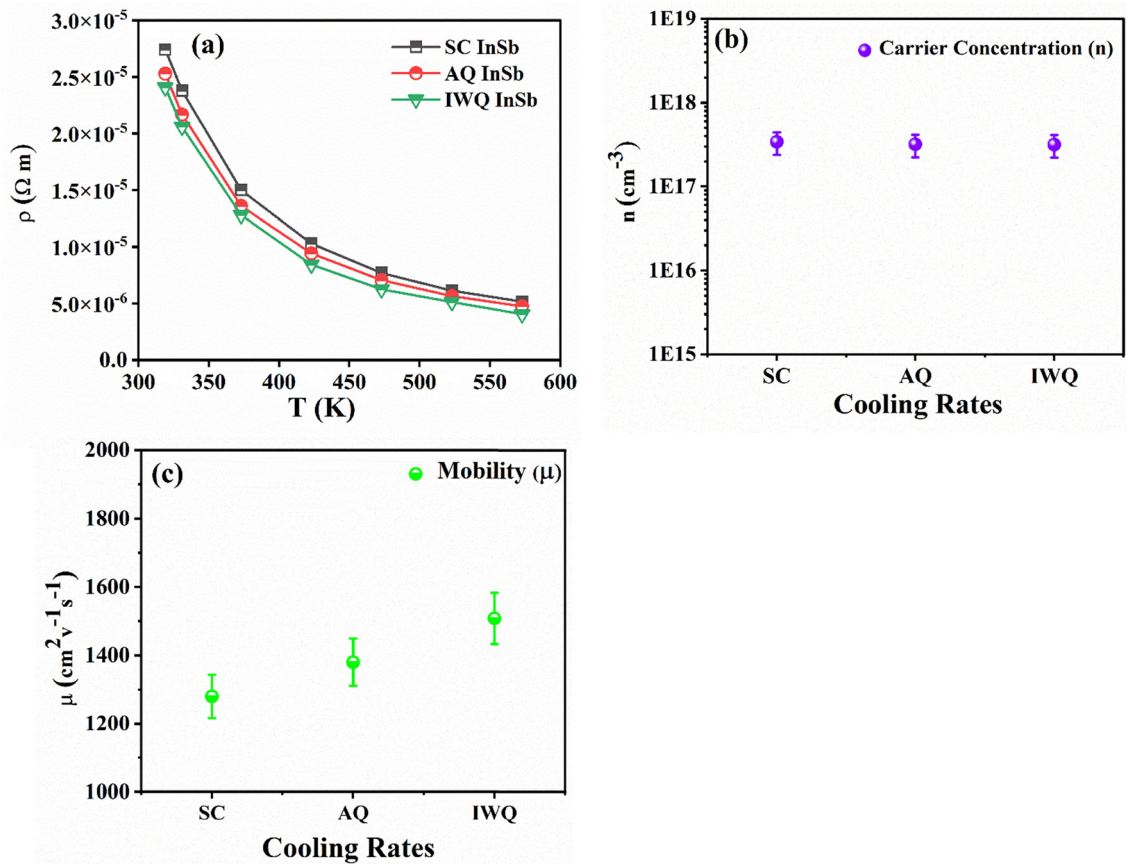

Fig. 5 Variation of ρ (as a function of temperature) (a), n (b) and μ (c) of SC InSb, AQ InSb and IWQ InSb samples.

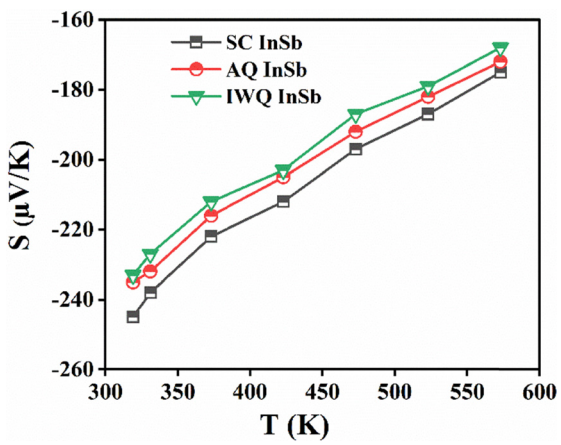

Fig. 6 Seebeck coefficient of SC InSb, AQ InSb and IWQ InSb samples.

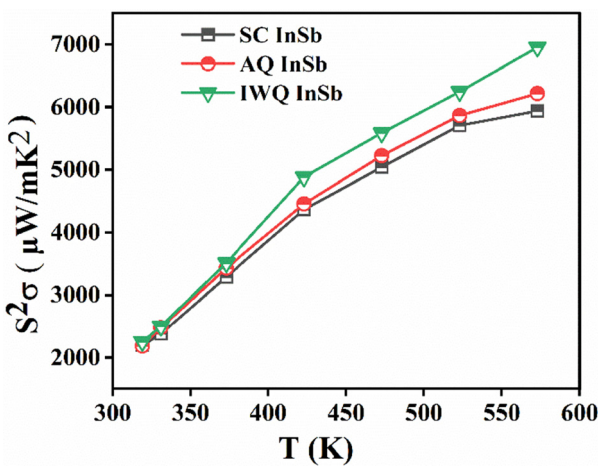

Fig. 7 Temperature-dependent power factors of SC InSb, AQ InSb and IWQ InSb samples.

with increasing cooling rate due to the low ρ values of the samples. The SC InSb shows a high S of -245 μV K^{-1} at 319 K compared to IWQ InSb (-233 μV K^{-1} at 319 K). The decrease in S with increasing temperature is attributed to intrinsic carrier excitation and the resulting bipolar conduction in narrow bandgap InSb, where thermally generated minority carriers reduce the net S through carrier compensation.

3.6 Thermoelectric power factor of the InSb samples

The PF of the samples was calculated from the measured S and ρ values at different temperatures. Fig. 7 shows the variations in the PF of InSb samples prepared at different cooling rates. A high PF of 6951 μW m^{-1} K^{-2} was achieved for IWQ InSb at 573 K

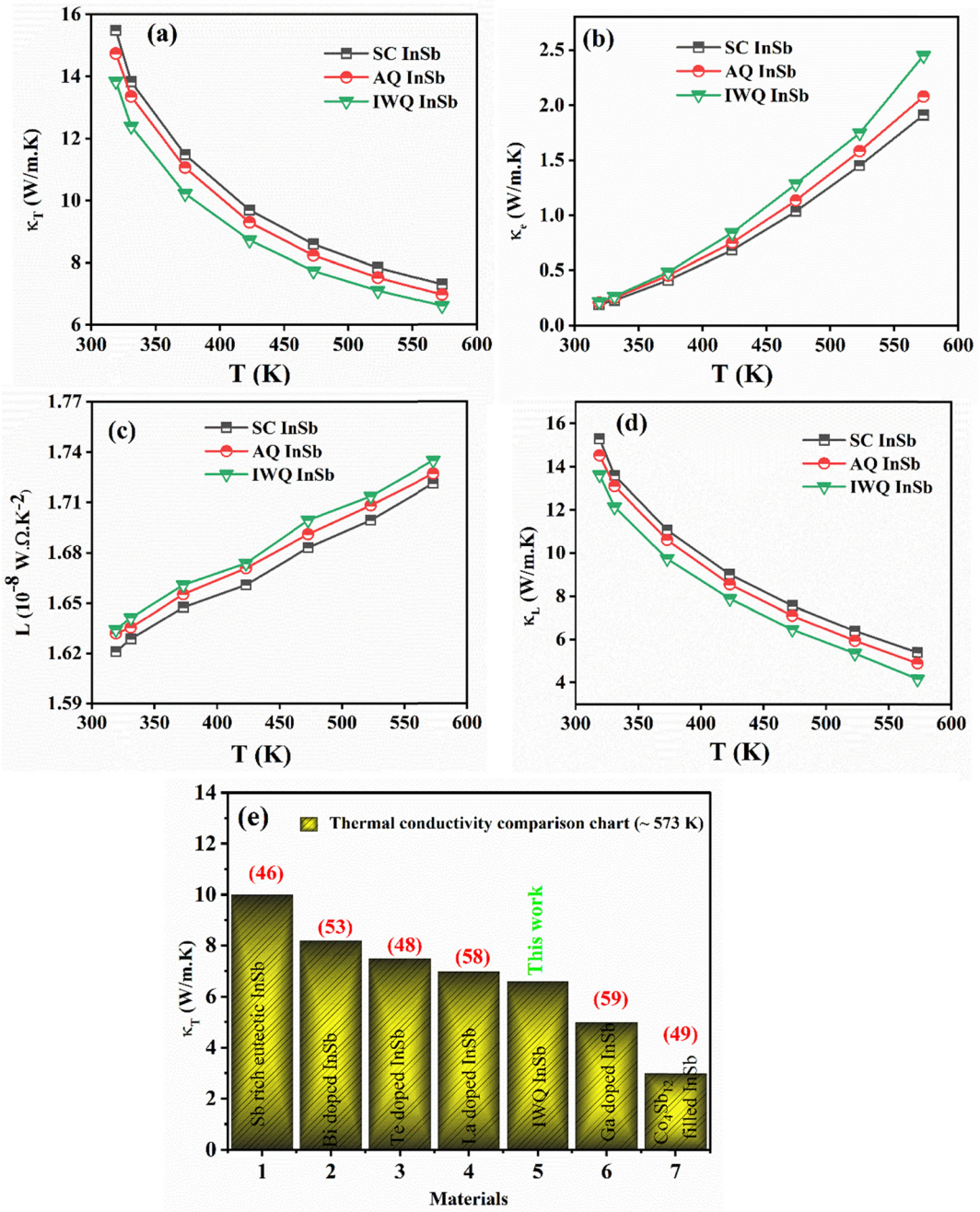

Fig. 8 (a)–(e) Total thermal conductivity (κ_T) (a), electronic thermal conductivity (κ_e) (b), lattice thermal conductivity (κ_L) (c), and temperature-dependent Lorentz number (L) (d) of InSb samples with cooling rates as a function of temperature and thermal conductivity comparison for various reported values (e).

compared to the SC InSb sample (5935 μW m^{-1} K^{-2} at 573 K). The low ρ values of the fine grain structured IWQ InSb sample resulted in higher PF compared to the other samples.

3.7 Thermal conductivity measurement of InSb

Fig. 8(a) displays the κ_T of various cooled InSb samples with respect to temperature. The κ_T is the combination of electronic thermal conductivity (κ_e) and lattice thermal conductivity (κ_T), which is represented using the following equation:[55,56]

$$\kappa_T = \kappa_e + \kappa_L. \quad (4)$$

The κ_T decreased as the cooling rate of the samples increased. The SC InSb has the κ_T of 7.29 W m^{-1} K^{-1} at 573 K, and it reduces to 6.60 W m^{-1} K^{-1} at the same temperature for the IWQ InSb. Fig. 8(b) shows the κ_e of the InSb samples at various temperatures. The κ_e was calculated using the following equation:

$$\kappa_e = \frac{LT}{\rho}. \quad (5)$$

The κ_e increased due to decrease in the ρ of the samples with the cooling rate. Fig. 8(c) shows the temperature-dependent

Lorentz number (L) of the prepared InSb samples at different cooling rates. The magnitude of L was calculated using the measured S values and their relations, as shown in the following equation (eqn (6)):[55,56]

$$L = 1.5 + \exp\left\{-\frac{|s|}{116}\right\}. \quad (6)$$

The L was increased as a function of the cooling rate due to the decrease in ρ.

Fig. 8(d) illustrates the κ_L of the InSb samples as a function of temperature. The κ_L was extracted by subtracting the κ_e from κ_T, using the following equation:[57]

$$\kappa_L = \kappa_T - \kappa_e = \kappa_T - \frac{LT}{\rho}. \quad (7)$$

The κ_L decreased as the cooling rates of the sample increased. The κ_L decreased with increasing temperature due to enhanced phonon–phonon Umklapp scattering, reducing the phonon mean free path at elevated temperatures. In addition, the EBSD images confirm a systematic reduction in grain size at the centres and edges from 910 μm and 905 μm in the SC InSb sample to 213 μm and 158 μm in the IWQ sample, respectively, leading to a significant increase in grain boundary density. These grain boundaries act as effective phonon scattering centers, further limiting thermal transport. The combined effect of intrinsic phonon–phonon scattering and extrinsic grain boundary scattering results in a pronounced suppression of κ_L, particularly in the fine-grain structured IWQ InSb samples. The grain boundary character distributions of the SC InSb, AQ InSb, and IWQ InSb samples are shown in Table S4 (a)–(c). SC InSb contains only low-angle Σ3 and Σ9 boundaries, resulting in weaker phonon scattering and higher lattice thermal conductivity (κ_l). In the AQ InSb sample, additional high-angle boundaries (Σ27a, Σ27b, and Σ19a) were present, which enhanced phonon scattering and reduced κ_L. IWQ InSb contains the highest fraction of higher angle boundaries (Σ27a, Σ27b, Σ35b, and Σ19b), leading to the strongest phonon scattering, which resulted in the lowest κ_L among all samples. Fig. 8(e) shows the thermal conductivity comparisons with the reported values of similar materials.[46,48,49,53,58,59] The measured thermal conductivity of the samples is relatively lower than that of the reported values.

Furthermore, as evident from XRD analysis, the increased structural disorder promotes phonon scattering, leading to reduced κ_L. The broadening of peaks and lower wavenumber shifts in the Raman spectra (Fig. 4) further confirm the lattice distortion in the IWQ sample compared to the SC sample. As shown in EBSD images (Fig. 3(a_1)–(c_2)), the IWQ InSb sample has smaller-sized grains compared to the SC InSb sample. As a result, the IWQ InSb sample has a greater number of grain boundaries, as shown in Fig. 3(c_1) and (c_2), which are responsible for effective scattering of phonons, leading to decreased κ_L. A schematic of the phonon scattering mechanism is shown in Fig. 9.

3.8 Figure of merit of InSb ingots with different cooling rates

Fig. 10(a) demonstrates the zT value of the prepared InSb samples with various cooling rates as a function of temperature. The zT was calculated using the PF and κ_T as a function of temperature. To obtain a high zT value, an extremely high PF and low κ_L are essential. Among all the samples, the IWQ InSb sample shows high PF and low κ_L. As a result, a higher zT value of 0.60 was achieved at 573 K for the IWQ InSb sample compared to the SC InSb sample (zT of 0.46 at 573 K). The zT values were compared with those of previous studies, as shown in Fig. 10(b).[46,48,49,53,58,59] The obtained zT values are relatively higher than those of previously reported similar materials.

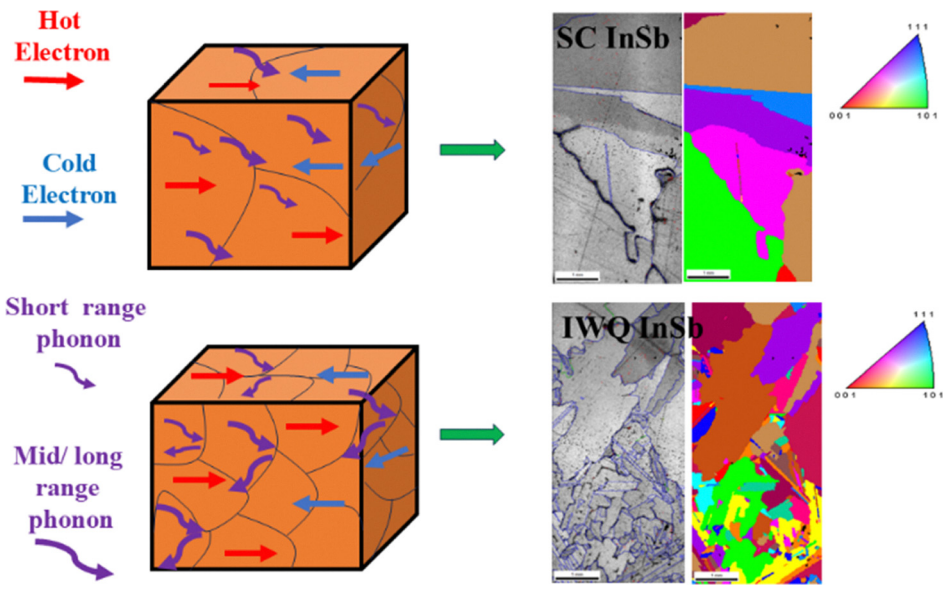

Fig. 9 Schematic of phonon scattering mechanisms for the SC InSb and IWQ InSb samples.

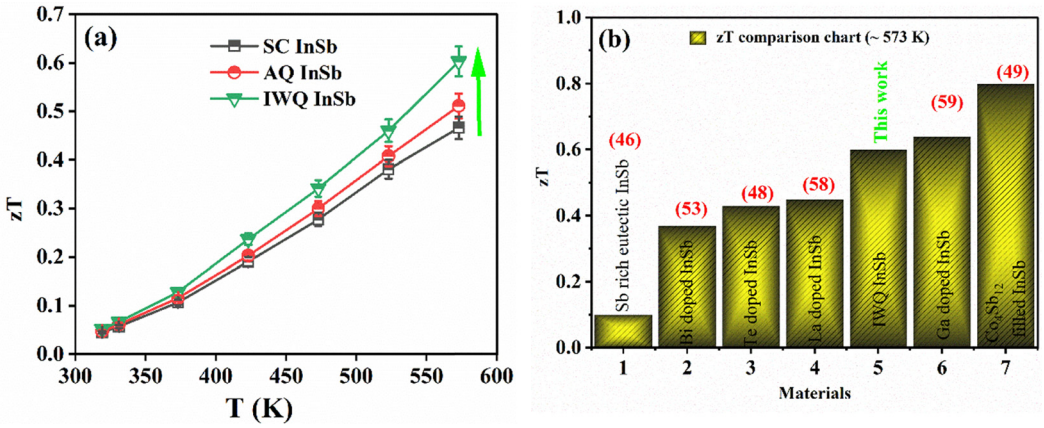

Fig. 10 *zT* value of InSb samples (a) with cooling rate as a function of temperature and comparison chart for various reported studies (b).

4. Conclusion

The polycrystalline InSb samples were prepared using the melt quenching technique at different cooling rates. The structural and surface morphological investigation of the samples was extensively carried out using XRD and FESEM. The ρ slightly decreased with increasing cooling rates. The S of the prepared InSb samples was measured up to 573 K. A high PF of 6951 μW m^{-1} K^{-2} was achieved for the IWQ InSb sample at 573 K compared to the SC InSb sample (5935 μW m^{-1} K^{-2} at 573 K). κ_T is reduced for the IWQ InSb sample (6.60 W m^{-1} K^{-1}) compared to SC InSb (7.29 W m^{-1} K^{-1}) at 573 K due to modification in the grain structures and grain boundary densities, which enhanced the phonon scattering in the IWQ sample. As a result, a high *zT* value of 0.60 was achieved at 573 K for the IWQ InSb sample compared to the SC InSb sample (*zT* of 0.46 at 573 K). The experimental results demonstrate that grain structure modification through the melt quenching process is an effective approach for enhancing the TE performance of InSb.

Author contributions

M. Sivakumar: conceptualization, methodology, formal analysis, investigation, validation, data curation, writing – original draft. J. Prasath: formal analysis, investigation. S. Senthamizh Raja: investigation, formal analysis. R. Annie Victoria Rose: formal analysis, investigation. J. Mani: formal analysis, investigation. L. C. Chuang: formal analysis, investigation, validation. Sri Sai Samhitha Gadhavajhala: formal analysis, data curation. Bhuvanesh Srinivasan: investigation, formal analysis, writing – review & editing. R. Jayavel: resources, writing – review & editing. K. Fujiwara: formal analysis, investigation, writing – review & editing, validation. M. Arivanandhan: conceptualization, project administration, resources, writing – review & editing, supervision.

Conflicts of interest

There are no conflicts to declare.

Data availability

The data supporting the findings of this study are available within the article and its supplementary information (SI). Supplementary information is available. See DOI: https://doi.org/10.1039/d6ma00062b.

Additional raw data are available from the corresponding author upon reasonable request.

Acknowledgements

This work was supported by the DST-INSPIRE Fellowship with INSPIRE code IF200541 awarded to M. S. The author M. S. would like to acknowledge the support from the Department of Science and Technology (DST), New Delhi, Government of India, for the award of DST Inspire Fellowship (Reference No: DST/INSPIRE FELLOWSHIP/2020/IF200541). The work is financially supported by the GIMRT collaborative project (202308-RDKGE-0536, 202408-RDKGE-0534), Tohoku University, Sendai, Japan. S. S. S. G. thanks PMRF for the fellowship. B. S. thanks the Anusandhan National Research Foundation (ANRF/erstwhile SERB) for the funding (File Numbers SRG/2023/002282 and CRD/2024/000912) and IIT-Madras for the seed grant (NFSG).

References

1 Y. Li, X. Wang, D. Luo, Y. Shi, Y. Ren and Y. Yan, *e-Prime – Adv. Electr. Eng. Electron. Energy*, 2023, **4**, 100180.
2 T. Hong, C. Guo, D. Wang, B. Qin, C. Chang, X. Gao and L. D. Zhao, *Mater. Today Energy*, 2022, **25**, 100985.
3 Z. G. Chen, G. Hana, L. Yanga, L. Cheng and J. Zou, 2012, preprint, DOI: 10.1016/j.pnsc.2012.11.011.
4 L. Wang, T. Chu, S. Yuan, P. Zou, W. Zhai, X. Zheng and M. Xia, 2025, preprint, DOI: 10.1016/j.enconman.2025.119621.
5 A. P. Sobha and S. K. Narayanankutty, *IEEE Trans. Nanotechnol.*, 2014, **13**, 835–841.
6 O. Caballero-Calero, J. R. Ares and M. Martín-González, 2021, preprint, DOI: 10.1002/adsu.202100095.

7 H. Mamur, Ö. F. Dilmaç, J. Begum and M. R. A. Bhuiyan, 2021, preprint, DOI: 10.1016/j.clema.2021.100030.
8 R. Singh, S. Dogra, S. Dixit, N. I. Vatin, R. Bhardwaj, A. K. Sundramoorthy, H. C. S. Perera, S. P. Patole, R. K. Mishra and S. Arya, 2024, preprint, DOI: 10.1016/j.hybadv.2024.100176.
9 Y. Liu, G. Song, K. Tai, Z. Yu, Y. Ran, J. He and Y. Wu, *Thin Solid Films*, 2025, **809**, 140585.
10 L. Huang, Y. Zheng, L. Xing and B. Hou, 2023, preprint, DOI: 10.1016/j.tsep.2023.102064.
11 S. H. Zaferani, M. W. Sams, R. Ghomashchi and Z. G. Chen, 2021, preprint, DOI: 10.1016/j.nanoen.2021.106572.
12 Z. Zhou, J. Yang, Q. Jiang, Y. Luo, D. Zhang, Y. Ren, X. He and J. Xin, *J. Mater. Chem. A*, 2016, **4**, 13171–13175.
13 A. Sampathu, M. Sivakumar, R. Chellakumar, D. Narendran, J. Kasthuri, S. Kumaran, M. Arivanandhan and M. Balakrishnan, *Mater. Sci. Semicond. Process.*, 2025, **204**, 110284.
14 P. H. M. Böttger, K. Valset, S. Deledda and T. G. Finstad, *J. Electron. Mater.*, 2010, **39**, 1583–1588, DOI: 10.1007/s11664-010-1269-2.
15 R. Annie Victoria Rose, D. Sidharth, M. Sivakumar, J. Kasthuri, B. Srinivasan, R. Jayavel and M. Arivanandhan, *ChemPhysChem*, 2025, **26**, e202500395.
16 Y. Yu, C. Zhou, T. Ghosh, C. F. Schön, Y. Zhou, S. Wahl, M. Raghuwanshi, P. Kerres, C. Bellin, A. Shukla, O. Cojocaru-Mirédin and M. Wuttig, *Adv. Mater.*, 2023, **35**, 2300893.
17 Q. Xiong, G. Han, G. Wang, X. Lu and X. Zhou, 2024, preprint, DOI: 10.1002/adfm.202411304.
18 Q. Jian, Y. Gong, C. Chen, R. Sun, S. Zhao, T. Shen, Q. Zhang, Y. Geng, Y. Li, W. Dou, C. Liang, Y. Liu, D. Xiang, P. Ying and G. Tang, *ACS Appl. Mater. Interfaces*, 2025, **17**, 15527–15534.
19 J. Chen, L. Wang, D. Ren, Y. Chu, Y. Wu, K. Meng, J. Miao, X. Xu and Y. Jiang, *Synth. Met.*, 2018, **239**, 13–21.
20 W. Li, Z. Yu, C. Liu, Y. Peng, B. Feng, J. Gao, G. Wu, X. Bai, J. Chen, X. Wang and L. Miao, *J. Adv. Ceram.*, 2023, **12**, 1511–1520.
21 L. L. Huang, J. Zhang, Z. M. Wang, X. G. Zhu, J. M. Li, C. Zhu, D. Li, C. J. Song, H. X. Xin and X. Y. Qin, *Materialia*, 2018, **3**, 169–173.
22 L. Xie, H. Tong, G. Peng, H. Wu, W. Shi, K. Yu, J. Hu, L. Jiao, X. Dong, F. Guo, W. Cai, Y. Zhang, H. Wu, Z. Liu and J. Sui, *Nat. Commun.*, 2025, **16**, 7484.
23 V. C. S. Theja, V. Karthikeyan, D. S. Assi, H. Huang, C. H. Shek and V. A. L. Roy, *Adv. Energy Sustainability Res.*, 2023, **4**, 2300125.
24 V. P. Kannan, V. Lourdhusamy, I. Paulraj, C. J. Liu and M. Sridharan, *ACS Appl. Mater. Interfaces*, 2023, **15**, 47058–47069, DOI: 10.1021/acsami.3c10418.
25 S. Perumal, S. Roychowdhury and K. Biswas, *Inorg. Chem. Front.*, 2016, **3**, 125–132.
26 Q. Wang, Z. Li, L. Xu, T. Jiang, J. Wang, X. Qian and S. Wang, *Mater. Today Phys.*, 2022, **27**, 100818.
27 Q. Zhang, Z. Xiong, J. Jiang, W. Li, G. Xu, S. Bai, P. Cui and L. Chen, *J. Mater. Chem.*, 2011, **21**, 12398–12401.
28 Y. Luo, J. Yang, Q. Jiang, W. Li, Y. Xiao, L. Fu, D. Zhang, Z. Zhou and Y. Cheng, *Nano Energy*, 2015, **18**, 37–46.
29 C. Wang, D. Cong, G. Tang, X. Zhou and J. Li, *Chem. Eng. J.*, 2024, **496**, 154313.
30 Q. Q. Wang, K. F. Liu, Y. Y. Su, X. C. Liu, Q. Liu, S. Zhou, J. Liu and S. Q. Xia, *Acta Mater.*, 2023, **255**, 119028.
31 K. Zhang, Y. Huang, S. Liu, Q. Xiong, S. Zheng, B. Zhang, G. Wang, Y. Pan, G. Han, G. Wang, X. Lu, X. Chen and X. Zhou, *Adv. Mater.*, 2025, **37**, 2503496.
32 N. Grevtsov, E. Chubenko, V. Bondarenko, I. Gavrilin, A. Dronov, S. Gavrilov, D. Goroshko, O. Goroshko, G. Rymski and K. Yanushkevich, *Mater. Res. Bull.*, 2025, **184**, 113258.
33 T. Zhu, K. Swaminathan-Gopalan, K. Stephani and E. Ertekin, *Phys. Rev. B*, 2018, **97**, 174201.
34 T. Palasyuk, C. Jastrzebski, A. Khachapuridze, E. Litwin-Staszewska, T. Suski, I. Grzegory and S. Porowski, *Phys. Status Solidi RRL*, 2024, **18**, 2400093.
35 R. Abinaya, J. Archana, S. Harish, M. Navaneethan, C. Muthamizhchelvan, S. Ponnusamy, H. Udono, R. Sugahara, Y. Hayakawa and M. Shimomura, *J. Colloid Interface Sci.*, 2021, **584**, 295–309.
36 D. K. Meena, R. S. C. Bose, S. Vinoth, K. Annapurna and K. Ramesh, *Appl. Phys. A*, 2022, **128**, 528.
37 X. Tang, Z. Li, W. Liu, Q. Zhang and C. Uher, 2022, preprint, DOI: 10.1002/idm2.12009.
38 J. D. Henderson, L. Pearson, H. Y. Nie and M. C. Biesinger, *Surf. Interface Anal.*, 2025, **57**, 81–97.
39 A. Vishwakarma, N. S. Chauhan, R. Bhardwaj, K. K. Johari, S. R. Dhakate, B. Gahtori and S. Bathula, *J. Electron. Mater.*, 2021, **50**, 364–374.
40 S. Perumal, M. Samanta, T. Ghosh, U. S. Shenoy, A. K. Bohra, S. Bhattacharya, A. Singh, U. V. Waghmare and K. Biswas, *Joule*, 2019, **3**, 2565–2580.
41 C. Liu, Z. Zhang, Y. Peng, F. Li, L. Miao, E. Nishibori, R. Chetty, X. Bai, R. Si, J. Gao, X. Wang, Y. Zhu, N. Wang, H. Wei and T. Mori, *Charge transfer engineering to achieve extraordinary power generation in GeTe-based thermoelectric materials*, 2023.
42 V. Nirmal Kumar, Y. Hayakawa, H. Udono and Y. Inatomi, *Intermetallics*, 2019, **105**, 21–28.
43 Y. Chen, X. L. Shi, D. Li, J. Zhu, M. Li, L. Zhang, Z. Zhang, Z. Feng, X. Ma, H. Zhong, S. Li and Z. G. Chen, *Acta Mater.*, 2025, **286**, 120736.
44 M. Jin, X. Bai, Z. Tang, S. Zhao, Y. Chen, L. Zhou, Y. Peng, X. Chen and X. Xu, *Mater. Res. Bull.*, 2021, **142**, 111411.
45 D. Besson, M. Treilleux, A. Hoareau and C. Esnouf, *Philos. Mag. A*, 2000, **80**, 1139–1149.
46 Y. Cheng, J. Yang, Q. Jiang, D. He, J. He, Y. Luo, D. Zhang, Z. Zhou, Y. Ren and J. Xin, *J. Mater. Chem. A*, 2017, **5**, 5163–5170.
47 K. Wang, P. Qin, Z. H. Ge and J. Feng, *Mater. Lett.*, 2017, **209**, 373–375.
48 S. Yamaguchi, T. Matsumoto, J. Yamazaki, N. Kaiwa and A. Yamamoto, *Appl. Phys. Lett.*, 2005, **87**, 1–3.
49 S. Ghosh, S. M. Valiyaveettil, G. Shankar, T. Maity, K. H. Chen, K. Biswas, S. Suwas and R. C. Mallik, *ACS Appl. Energy Mater.*, 2020, **3**, 635–646.
50 W. Li, T. Xu, Z. Ma, Y. Cheng, J. Li, Q. Jiang, Y. Luo and J. Yang, *Mater. Today Energy*, 2022, **29**, 101091.
51 M. Sivakumar, D. Sidharth, B. Srinivasan and M. Arivanandhan, *J. Alloys Compd.*, 2024, **1009**, 176908.

52 L. L. Huang, J. Zhang, Z. M. Wang, X. G. Zhu, J. M. Li, C. Zhu, D. Li, C. J. Song, H. X. Xin and X. Y. Qin, *Materialia*, 2018, **3**, 169–173.
53 J. Palraj, M. Moorthy, S. Katlakunta and S. Perumal, *Ceram. Int.*, 2022, **48**, 29284–29290.
54 Z. Lu, B. Huang, G. Li, X. Zhang, Q. An, B. Duan, P. Zhai, Q. Zhang and W. A. Goddard, *npj Comput. Mater.*, 2021, **7**, 111.
55 R. Annie Victoria Rose, D. Sidharth, M. Arivanandhan and R. Jayavel, *New J. Chem.*, 2024, **48**, 11506–11517.
56 D. Sidharth, I. Paulraj, V. Lourdhusamy, M. Arivanandhan and C. J. Liu, *J. Eur. Ceram. Soc.*, 2024, **44**, 954–960.
57 D. Sidharth, B. Srinivasan, A. S. A. Nedunchezhian, P. Thirukumaran, M. Arivanandhan and R. Jayavel, *J. Phys. Chem. Solids*, 2022, **160**, 110303.
58 D. Zhang, H. Wu, Z. Zhou, S. Zheng, B. Zhang, Y. Zhou, X. Lu and X. Zhou, *Mater. Today Phys.*, 2023, **32**, 101020.
59 Z. Du, X. Chen, J. Zhu and J. Cui, *Curr. Appl. Phys.*, 2018, **18**, 893–897.